Polymorphic $PtBi_2$: Growth, structure, and superconducting properties

G. Shipunov,[1,*] I. Kovalchuk,[1,2] B. R. Piening,[1] V. Labracherie,[1] A. Veyrat,[1] D. Wolf,[1] A. Lubk,[1] S. Subakti,[1] R. Giraud,[1,3] J. Dufouleur,[1] S. Shokri,[1] F. Caglieris,[1] C. Hess,[1] D. V. Efremov,[1] B. Büchner,[1,4] and S. Aswartham[1,†]

[1]*Leibniz Institute for Solid State and Materials Research Dresden, Helmholtzstrasse 20, D-01069 Dresden, Germany*

[2]*Kyiv Academic University, 03142 Kyiv, Ukraine*

[3]*Université Grenoble Alpes, CNRS, CEA, Spintec, F-38000 Grenoble, France*

[4]*Institut für Festkörperphysik, TU Dresden, D-01062 Dresden, Germany*

(Received 25 February 2020; revised 2 October 2020; accepted 5 November 2020; published 3 December 2020)

$PtBi_2$ is a polymorphic system with interesting electronic properties. Here we report optimized crystal growth and structural characterization of pyrite-type and trigonal modification of $PtBi_2$. Selected area electron diffraction, x-ray powder diffraction, and further Rietveld refinement confirms that trigonal $PtBi_2$ crystallizes in the noncentrosymmetric $P31m$ space group, and pyrite-type $PtBi_2$ crystallizes in the $Pa\bar{3}$ space group. A series of $Pt_{1-x}Rh_xBi_2$ samples was obtained for $x = 0, 0.03, 0.35$ in the trigonal $PtBi_2$ structure. These $Pt_{1-x}Rh_xBi_2$ compounds become superconducting where the critical temperature increases from $T_c = 600$ mK for $x = 0$ up to $T_c = 2.7$ K for $x = 0.35$. Furthermore, we calculate the electronic band structure using the obtained structure parameters. The calculated density of states shows a minimum for the stoichiometric compound at the Fermi level. These findings warrant further research using a broader array of experimental techniques, as well as on the effect of the substitution on the nontrivial band structure.

DOI: 10.1103/PhysRevMaterials.4.124202

I. INTRODUCTION

Topological materials (TMs) are a new class of quantum materials, which are characterized by a nontrivial topological band structure [1]. After the initial discovery of such properties in the family of topological insulators, many other types of TMs followed, including Dirac and Weyl types of topological semimetals (TSMs), which are characterized by conduction- and valence-band touching at several points near the Fermi level and show linear electron dispersion near those points, which are termed Dirac and Weyl nodes, respectively [2,3]. The presence of these points was experimentally detected by angle-resolved photoemission spectroscopy (ARPES) measurements as Fermi arcs [4]. These topological bands strongly influence charge transport properties, such as electron mobility, giant magnetoresistance, and the anomalous Hall effect [5–9]. The combination of the nontrivial band structure with superconductivity in the same system makes it even more interesting due to the possibility of realization of Majorana fermions [10].

In recent years, $PtBi_2$ has attracted a lot of attention from the scientific community as one of the members of TSM family, which, together with the report of superconductivity in the system [11], makes it an attractive candidate for topological superconductivity. It crystallizes in four polymorphic modifications [12]: δ, which could be formed by a peritectic reaction at 660 °C and is thermodynamically stable down to 640 °C; the temperature range of 420–640 °C corresponds to the γ modification [12,13]; in between 270 and 420 °C, the β modification is thermodynamically favorable; and the final polymorphic transition into the α modification is at the temperature around 270 °C [12,14].

Two of these modifications, β (cubic, usually referred as pyrite type) and γ (hexagonal, referred as trigonal below), were recently shown to exhibit interesting physical properties. Pyrite-type $PtBi_2$ (space group $Pa\bar{3}$) shows extremely large unsaturated magnetoresistance, superseding the values demonstrated by WTe_2 [15], and has been proposed to host Dirac fermions [16]. Further, multiband superconductivity with perfect electron-hole compensation under high pressure was reported [17]. Pyrite-type $PtBi_2$ was reported to host a sixfold fermion near the Fermi level, with confirmation from ARPES [18]. Trigonal polymorph is an example of a layered van der Waals material, namely, two-dimensional (2D) layers of covalently bound Pt and Bi are held together weakly, which makes this system a promising candidate for thickness-dependent studies due to the ease of exfoliation. This modification also shows large magnetoresistance [19]; however, no superconductivity was reported for this modification. There are different reports on the theoretical band structure of trigonal $PtBi_2$: some reports assume centrosymmetric space group $P\bar{3}$ [20–22], while in Ref. [21], the noncentrosymmetric space group $P31m$ was assumed. Both structure variations were previously reported with the same lattice parameters: $a = 6.57$ Å, $c = 6.16$ Å for $P\bar{3}$ [14] (ICSD No. 58847) and $a = 6.573$ Å, $c = 6.167$ Å for $P31m$ [23] (ICSD No. 428088); images of the reported structures are presented in Fig. 1 for clarity. In the $P\bar{3}$ model, Pt atoms are laid out in a corrugated triangular lattice, with every Pt atom coordinated by six atoms of Bi, while in the $P31m$ model,

*g.shipunov@ifw-dresden.de
†s.aswartham@ifw-dresden.de

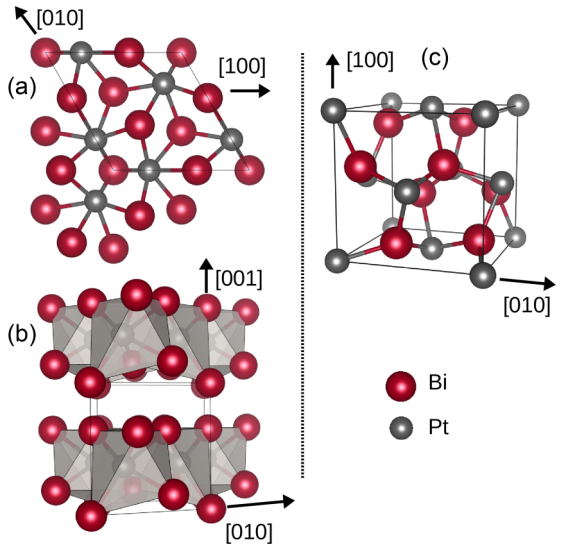

FIG. 1. Reported structures of (a),(b) trigonal and (c) pyrite-type polymorphs of $PtBi_2$. (a) Trigonal polymorph model in space group $P31m$ proposed in [23], for the view along [001]. (b) Same, for the view along [100]. (c) Reported structure of the pyrite-type polymorph of $PtBi_2$ (space group $Pa\bar{3}$) [25].

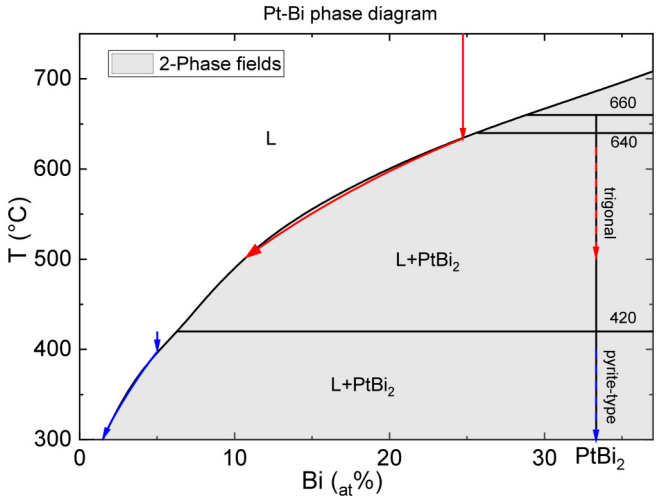

FIG. 2. The fragment of the published Pt-Bi phase diagram [12]. The arrows schematically represent the synthesis conditions for trigonal (red) and pyrite-type (blue) modification. The solid lines show the composition of the liquid phase during the synthesis, while the dashed lines show the composition of the precipitating solid phase.

the Pt position shifted towards the 3 axis to complete the Pt outer shell to magic number $18e^-$, which results in further deformation of the $PtBi_6$ octahedra and corrugation of Bi layers.

Trigonal modification of $PtBi_2$ was predicted to host Dirac fermions when described in the space group $P\bar{3}$ [20] or Weyl fermions and a triply degenerate point when described in the $P31m$ space group due to the absence of spatial inversion symmetry [24], so a distinction between the two is crucial for further investigation of the physical properties of the material. This, together with the fact that the predicted triply degenerate points are near the Fermi level [24], makes trigonal $PtBi_2$ an interesting material for probing the properties of such fermionic excitations.

The aim of the present article is to report the optimized synthesis conditions, to study the crystal structure and physical properties of pristine $PtBi_2$, as well as to study $PtBi_2$ with substitution of Pt by Rh. Substitution of Pt (with outer-shell configuration $5d^9$) by Rh ($4d^8$) produces overall hole doping, which should affect the density of states (DOS) near the Fermi level. The article is constructed as follows: in the first section, we report the optimized methods for crystal growth of both pyrite-type and trigonal modification. For trigonal modification, we study a series of crystals, $Pt_{1-x}Rh_xBi_2$, by means of scanning electron microscopy–energy dispersive x-ray spectroscopy (SEM-EDX), x-ray diffraction (XRD), selected area electron diffraction (SAED), superconducting quantum interference device (SQUID), and electrical transport measurements. Using the obtained parameters of the crystal structure, we find the electronic band structure for the trigonal polymorph in the framework of the density functional theory (DFT). Also we show the superconductivity in trigonal polymorph with the way to enhance the transition temperature by Rh substitution.

II. METHODS

A. Crystal growth

Single crystals of pyrite-type and trigonal $PtBi_2$ were grown via the self-flux method. All ampules, crucibles, and quartz wool were heat treated before the synthesis at 800 °C for 24 hours. The optimized temperatures were chosen according to the published Pt-Bi phase diagram [12] (a region of the phase diagram is presented in Fig. 2), such that crystallization happens only in the crystallization zone of the chosen polymorphic modification, preventing precipitation of unwanted modifications. According to the phase diagram, it is possible to selectively crystallize trigonal $PtBi_2$ from Bi flux in the temperature region between 420 and 640 °C with the corresponding Pt content of 7–26 at.% (red lines in Fig. 2), and for pyrite-type modification in the temperature region of 272–420 °C and Pt content under 7 at.% (blue lines in Fig. 2). For the $Pt_{1-x}Rh_xBi_2$ samples, due to the absence of a published ternary phase diagram, similar temperature ranges and flux-to-metal ratios were assumed. Small drops of flux residue were removed from the surface either mechanically or by etching in a HNO_3 dilute solution.

Trigonal modification. Single crystals of trigonal $PtBi_2$ and $Pt_{1-x}Rh_xBi_2$ were synthesized by mixing elemental powders of Pt (99.99%, Saxonia Edelmetalle GmbH), Rh (99.95%, Evochem), and Bi (325-mesh powder, 99.5%, Alfa Aesar). Elemental powders with molar ratio of $(Pt_{1-x}Rh_x) : Bi = 1 : 4$ (for $x = 0$, 0.1, and 0.3) and a total charge mass of 0.4 g were homogenized by manual grinding for 5 min in agate mortar and placed into a Canfield crucible set [26] to facilitate flux removal at a later stage. The crucible in turn was sealed inside of an evacuated quartz glass tube to prevent oxidation. For the unsubstituted compound, the setup then was heated to 850 °C at 100 °C/h and held at that temperature for 10 h. After that, the mixture was cooled to 420 °C with a rate of 2 °C/h, after which excess of the flux was removed by centrifugation.

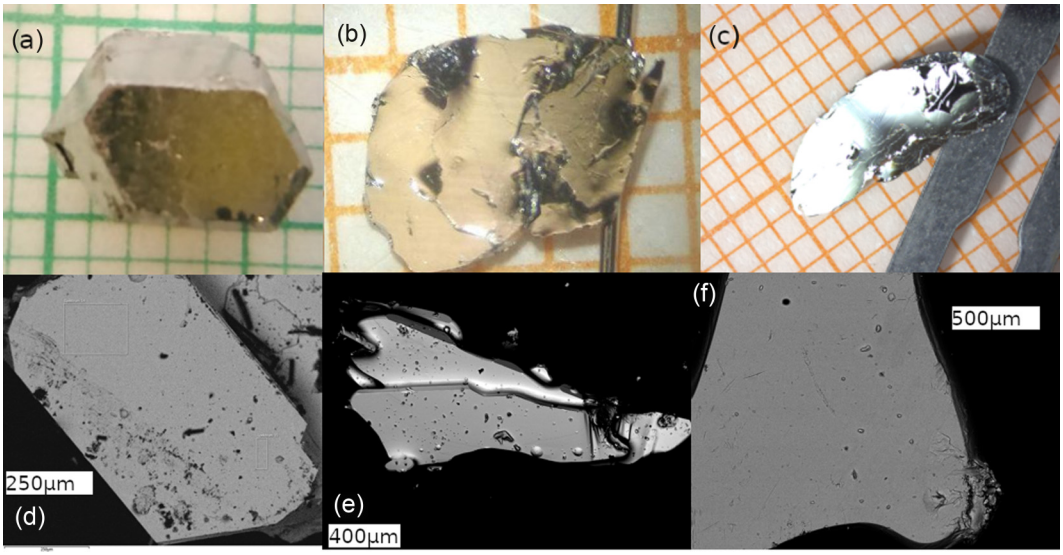

FIG. 3. As-grown crystals on a millimeter scale: (a) pyrite-type $PtBi_2$, (b) trigonal $PtBi_2$, and (c) $Pt_{0.65}Rh_{0.35}Bi_2$. SEM–backscattered electron (BSE) images: (d) $PtBi_2$ and (e),(f) $Pt_{0.65}Rh_{0.35}Bi_2$.

Rh-containing reaction mixtures were also heated to 850 °C at 100 °C/h with the same dwell time at a maximum temperature of 10 h, but due to the absence of phase diagram data in the ternary (Pt-Rh-Bi) system, the cooling step was shortened so it would not go below the temperature of 500 °C in order to prevent crystallization of hypothetical secondary phases. The as-grown crystals shown in Figs. 3(b) and 3(c) clearly demonstrate the layered morphology.

Pyrite-type modification. Crystals of $PtBi_2$ in a pyrite-type modification were obtained in a likewise manner: A mixture of elemental powders with molar ratio of Pt:Bi = 1 : 20 was homogenized by manual grinding in an agate mortar, placed into a Canfield crucible set, and sealed in a quartz ampule. The setup was heated to 400 °C at 100 °C/h, held at that temperature for 4 days, then cooled at 0.25 °C/h to 300 °C, with centrifugation of excess flux hereafter. The as-grown crystals are faceted and isometric, as shown in Fig. 3(a).

B. Characterization of composition and structure

The composition of the as-grown single crystals was determined by energy-dispersive x-ray spectroscopy (EDX), with an electron beam probe (accelerating voltage 30 kV, current 552 pA). Scanning electron microscopy images are shown in Figs. 3(d)–3(f). The structural characterization and phase purity were confirmed by means of powder x-ray diffraction using a STOE powder diffractometer (2θ:ω scan, Co $K_{\alpha 1}$ or Mo $K_{\alpha 1}$ radiation, curved Ge (111) monochromator, Debye-Scherrer geometry). Rietveld refinement of the x-ray data was carried out with the FULLPROF [27] and JANA2006 [28] software packages. Selected area electron diffraction (SAED) on $PtBi_2$ and $Pt_{1-x}Rh_xBi_2$ nanoflakes was performed on an FEI Tecnai G2 transmission electron microscope (Thermo Fisher Scientific) with an LaB_6 emitter operated at 200 kV acceleration voltage. The quality and stability of the $Pt_{1-x}Rh_xBi_2$ crystals used in this experiment allow us to carry out a mechanical exfoliation process using commercially available adhesive tape (Vivess). The tape and exfoliated $Pt_{1-x}Rh_xBi_2$ crystals were separated by immersion in 20 mL of acetone and isopropanol (1:1) solution in 50 mL beaker glass. Ultrasonic waves (frequency 35 KHz) were employed to assist the separation of the $Pt_{1-x}Rh_xBi_2$ flakes from the tape surface. The micrometer-size $Pt_{1-x}Rh_xBi_2$ flakes for transmission electron microscopy (TEM) characterizations were then transferred from the bottom of the beaker glass to the Cu grids using a standard pipette. To ensure the cleanliness of the $Pt_{1-x}Rh_xBi_2$ flakes for selected area diffraction investigation, we determined the elemental compositions of every $Pt_{1-x}Rh_xBi_2$ flake by *in situ* energy-dispersive X-ray spectroscopy before collecting the selected area diffraction-pattern data. Theoretical kinematic electron diffraction patterns were computed and visualized using the SINGLECRYSTAL software package, version 3.1.5 (CrystalMaker Software, UK).

C. Characterization of physical properties

In-plane resistivity measurements have been performed in a standard four-probe configuration. Electrical contacts have been made with copper or silver wires glued to the sample using a conducting silver paint (Dupont 4929n). The measurements have been performed in the temperature range 2.3–300 K in a liquid ^{4}He cryostat endowed with a 15 T magnet and in the temperature range 0.1–1 K using a dilation fridge in a liquid ^{4}He cryostat with a 3D vector magnet (6T-2T-2T).

The magnetization data were measured using a Quantum Design MPMS SQUID with a vibrating sample magnetometer. The electronic band structure was obtained in the framework of fully relativistic density functional theory (DFT) using the Full Potential Local Orbital band structure package (FPLO) [29]. The calculations were carried out within the generalized gradient approximation (GGA) of the Perdew-Burke-Ernzerhof (PBE) exchange-correlation potential [30]. A k mesh of $12 \times 12 \times 12$ k points in the whole Brillouin zone was employed.

TABLE I. Nominal compositions and compositions according to SEM-EDX for obtained $Pt_{1-x}Rh_xBi_2$ compounds.

Nominal	SEM-EDX
Cubic:	
$PtBi_2$	$PtBi_{2.00(2)}$
Trigonal:	
$PtBi_2$	$PtBi_{2.03(4)}$
$Pt_{0.9}Rh_{0.1}Bi_2$	$Pt_{0.97(1)}Rh_{0.02(1)}Bi_{1.89(2)}$
$Pt_{0.7}Rh_{0.3}Bi_2$	$Pt_{0.64(2)}Rh_{0.35(1)}Bi_{1.9(3)}$

III. RESULTS AND DISCUSSION

A. Composition and structure

Pyrite-type $PtBi_2$ was obtained as large, well-faceted, isometric silvery crystals up to 0.5 cm in diameter and a mass of up to 500 mg. As an example, one of the as-grown pyrite-type crystals is shown in Fig. 3(a). Crystals of trigonal $PtBi_2$ and $Pt_{1-x}Rh_xBi_2$ were obtained as easily cleavable silvery plates with a layered morphology in tabular hexagonal habit, which is in line with the layered van der Waals structure of the material. The crystals of size up to 5 × 10 mm and mass up to 200 mg were acquired as shown in Figs. 3(b) and 3(c).

An SEM-EDX analysis of both trigonal [for SEM images, see Figs. 3(d) and 3(e)] and pyrite-type modification of $PtBi_2$ confirmed the stoichiometric composition of the compounds and showed a homogenous distribution of the elements. Samples with substitution show uniform rhodium incorporation into the crystal. For 10% and 30% nominal substitution levels, the measured EDX composition is $Pt_{0.97(1)}Rh_{0.02(1)}Bi_{1.89(2)}$ and $Pt_{0.64(2)}Rh_{0.35(1)}Bi_{1.9(3)}$, respectively. The results of the EDX analysis are presented in Table I. The structure of pyrite-type $PtBi_2$ was determined by powder x-ray diffraction with subsequent Rietveld analysis. X-ray powder analysis shows no secondary phases and the obtained structural parameters agree well with those previously published with $a = 6.702$ in space group $Pa\bar{3}$ [25].

For trigonal modification, powder XRD data from crystals ground by hand show abnormally broad diffraction peaks. This behavior might be linked to the high ductility and ease of cleavage of the material. To obtain high-quality XRD data, crystals were ground in a ball mill for 30 min, and afterwards the powder was annealed at the centrifugation temperature, to relieve any internal stress caused by milling, and quenched in ambient-temperature water to prevent polymorphic transformation to pyrite-type modification. Since two slightly different crystal structures for the trigonal modification were reported in the literature with the same lattice parameters, our pattern was compared to the theoretically modeled one for $PtBi_2$ structures reported in the Inorganic Crystal Structure Database (ICSD) FIZ Karlsruhe GmbH [14,23]. The pattern shows the presence of a minor quantity of secondary phases. Those secondary phases were fitted with the Le Bail method prior to the Rietveld refinement to exclude them from consideration. The results of the Rietveld fit for trigonal $PtBi_2$ are presented in Figs. 4(a) and 4(b). We performed the analysis of the x-ray data employing both models presented in the literature: in $P\bar{3}$ [14] and $P31m$ [23]. While in both cases the lattice parameters agree with the data previously published, refinement in the $P\bar{3}$ space group gives rise to negative isotropic displacement parameters for the "Pt1" and "Bi1" positions. Moreover, the residual parameters for this model are considerably worse for the $P\bar{3}$ model (e.g., $R = 0.1163$ vs $R = 0.0520$ for the $P31m$ model). A comparison of the refinement results is presented in Table II. To further support this finding, selected area electron diffraction (SAED) on individual $Pt_{1-x}Rh_xBi_2$ flakes exfoliated from a single crystal was carried out (Fig. 5). The SAED patterns for $Pt_{1-x}Rh_xBi_2$ recorded in [001] ($x = 0$) and [012] ($x = 0.35$) orientation were compared with the theoretical patterns for both space groups $P\bar{3}$ [Figs. 5(a) and 5(c)] and $P31m$ [Figs. 5(b) and 5(d)]. The presence of the 200 and symmetrical equivalent reflections in the experimental data strongly suggest a $P31m$ space-group structure for both crystals. These reflections are forbidden in diffraction patterns computed from the $P\bar{3}$ space group, i.e., they have a three-orders-of-magnitude lower scattering factor compared to $P31m$ because of its lower symmetry.

As the sample is better described in the $P31m$ space group, structural investigation of both pristine and Rh-substituted samples was carried out employing this model. It is worth noting that the $P31m$ space group is not centrosymmetric, which makes it a theoretically proposed candidate for the realization of Weyl states [21] and an attractive system for studying the triply degenerate point fermions in that system [24].

Results of the refinement of a 3% substituted sample are presented in Fig. 4 and in Tables II and III. In the case of

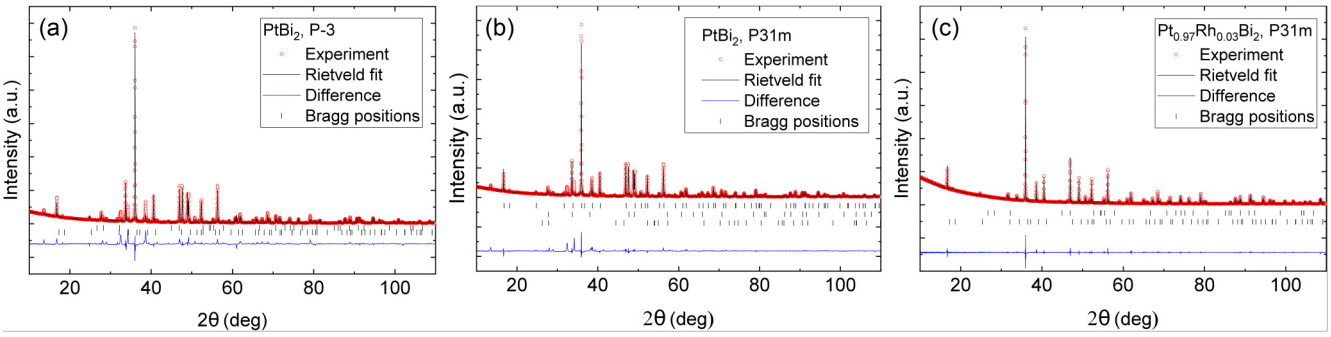

FIG. 4. Rietveld analysis of $Pt_{1-x}Rh_xBi_2$. For $x = 0$, using the model in the (a) $P\bar{3}$ space group [14] and (b) $P31m$ space group [23]. (c) Rietveld fit for $x = 0.03$ with the model in the $P31m$ space group.

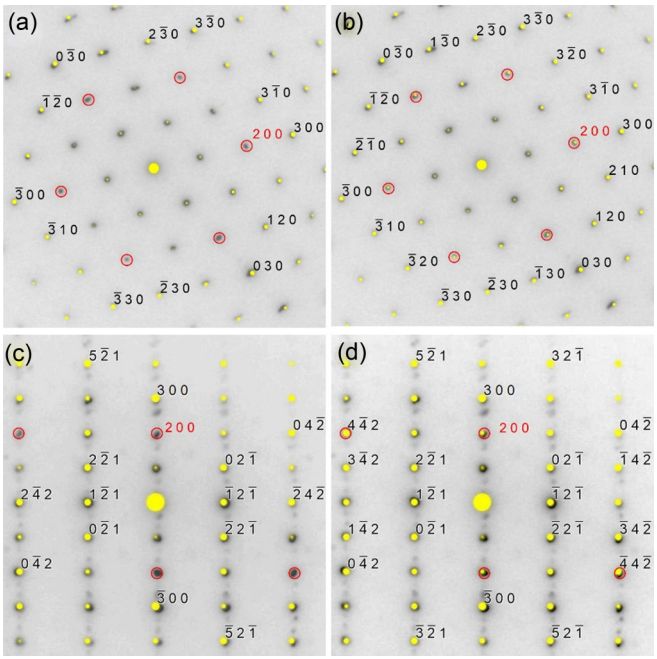

FIG. 5. Selected area electron diffraction (SAED) on $Pt_{1-x}Rh_xBi_2$. (a),(b) SAED pattern of a representative nanoflake ($x = 0$) oriented in the [001] zone axis overlaid with theoretical SAED patterns (yellow dots) using (a) $P\bar{3}$ and (b) $P31m$ space-group structure. (c),(d) SAED pattern of a representative nanoflake ($x = 0.35$) oriented in the [012] zone axis overlaid with theoretical SAED patterns (yellow dots) using (c) $P\bar{3}$ and (d) $P31m$ space-group structure. The red circles in (a)–(d) indicate the 200 and symmetrical equivalent reflections that are virtually forbidden for (a),(c) $P\bar{3}$ symmetry, but clearly show up for (b),(d) $P31m$.

the 3% substitution, refinement of the Rh/Pt occupational parameters from powder data is not feasible due to the low Rh content, so in the refinement model, the Pt1 position was set to be fully occupied by platinum. With the substitution of Pt by Rh, we observe a slight increase in the a parameter by $\Delta a \approx 0.003$ Å and a noticeable decrease of parameter c by $\Delta c \approx -0.02$ Å. This effect might be another indication of solid solution formation and can be explained by compression of distorted Bi octahedra and, as a result, slight expansion of the Pt-Bi framework in the ab plane. This lattice deformation might be a helpful tool to study Weyl point behavior since the position of such nodes in the electronic structure is quite sensitive to changes in the lattice parameters. Such lattice deformation might provide an effect analogous to strain which, according to theoretical models, can result in experimentally measurable effects [31], and it already was shown experimentally that substitution can enhance superconductivity in the sample [32].

TABLE II. Structural parameters and residual factors of Rietveld analysis.

	Composition	$Pt_{1-x}Rh_xBi_2$	x
Parameter		0	0.03
Wavelength (Å)	1.78996	1.78996	1.78996
2θ range (°)	10–111.955	10–111.955	10–111.995
Step Size (°)	0.015	0.015	0.015
Temperature (K)	293	293	293
Space group	$P\bar{3}$ (No. 147)	$P31m$ (No. 157)	$P31m$ (No. 157)
a (Å)	6.5731(8)	6.5731(6)	6.57696(2)
c (Å)	6.162(2)	6.1619(13)	6.14796(4)
$U_{isotropic}$:			
U_{Pt1}	−0.0857(14)	0.025(1)	0.0077(5)
U_{Pt2}	0.043(3)	n/a	n/a
U_{Bi1}	−0.0183(9)	0.052(2)	0.0164(9)
U_{Bi2}	n/a	0.0209(14)	0.0087(5)
U_{Bi3}	n/a	0.0218(10)	0.0142(5)
R	0.1163	0.0520	0.0226
wR	0.1892	0.0725	0.0324
Goodness of fit	8.45	6.68	1.92

TABLE III. Refined atomic coordinates for $Pt_{1-x}Rh_xBi_2$.

Sample	Atom	Site	x	y	z
$PtBi_2$	Pt (Pt1)	3c	0.2619(5)	0	0.363(13)
	Bi (Bi1)	1a	0	0	0
	Bi (Bi2)	2b	2/3	1/3	0.155(13)
	Bi (Bi3)	3c	0.6144(5)	0	0.630(13)
$Pt_{0.97}Rh_{0.03}Bi_2$	Pt/Rh (Pt1)	3c	0.2617(2)	0	0.3578(6)
	Bi (Bi1)	1a	0	0	0.0139(6)
	Bi (Bi2)	2b	2/3	1/3	0.1413(6)
	Bi (Bi3)	3c	0.6093(2)	0	0.6345(5)

B. Magnetization and Resistivity

Magnetization measurements in the temperature range of $T = 1.8$–300 K in the 0.5 T field show diamagnetic behavior for both parent and Rh-substituted compounds with a Curie tail region at low temperatures, perhaps due to some paramagnetic impurities. Figure 6 presents the temperature-dependent volume susceptibility (χ_{vol}) for the $Pt_{0.65}Rh_{0.35}Bi_2$ compound. χ_{vol} was deduced from the measured magnetization vs temperature dependence and has not been corrected for demagnetization effects. The sharp onset of the superconduct-

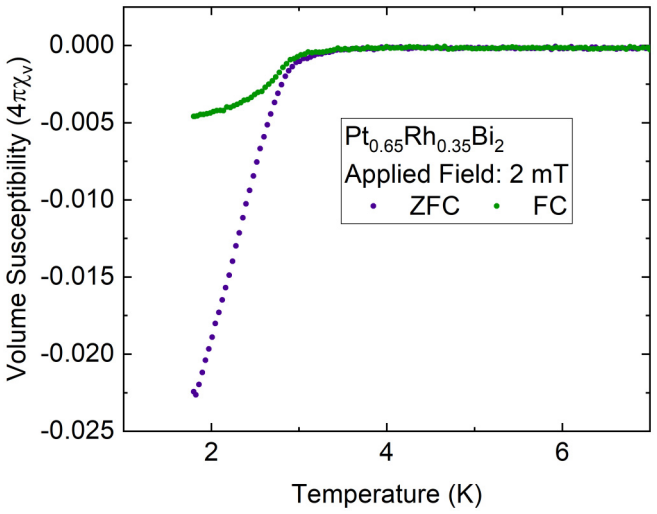

FIG. 6. Temperature dependence of volume susceptibility for $Pt_{0.65}Rh_{0.35}Bi_2$ in an applied field of $H||ab = 2$ mT.

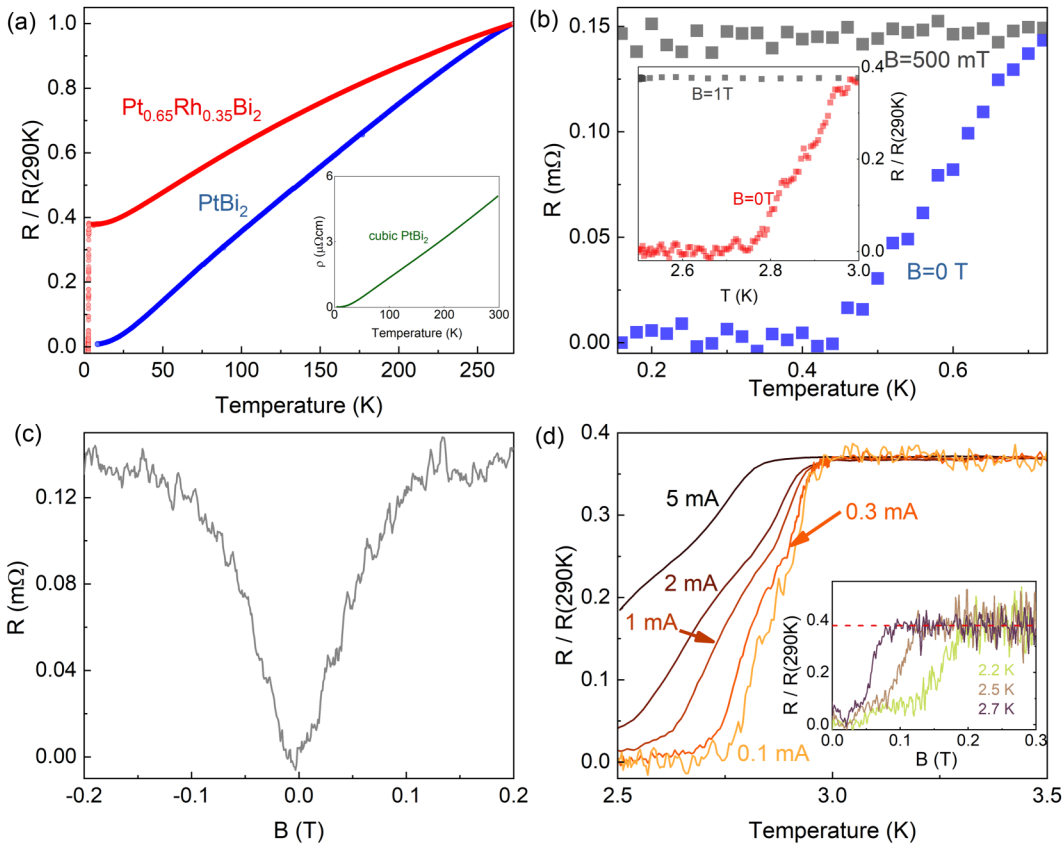

FIG. 7. (a) T-dependence of the normalized resistivity ρ/ρ_{290K} for trigonal $PtBi_2$ and $Pt_{0.65}Rh_{0.35}Bi_2$. Inset: T-dependence of the resistivity for cubic $PtBi_2$. (b) T-dependence of R for $PtBi_2$ with magnetic field $B = 0$ T and $B = 500$ mT, applied parallel to the c axis. Inset: T-dependence of ρ/ρ_{290K} for $Pt_{0.65}Rh_{0.35}Bi_2$ with magnetic field $B = 0$ and $B = 1$ T, applied parallel to the c axis. (c) B-dependence of R for $PtBi_2$ at $T = 100$ mK. (d) Low temperature ρ/ρ_{290K} vs T curves for $Pt_{0.65}Rh_{0.35}Bi_2$ with different applied current from 0.1 to 5 mA. Inset: Magnetic field dependence of ρ/ρ_{290K} for $Pt_{0.65}Rh_{0.35}Bi_2$ at different $T = 2.2$, 2.5, and 2.7 K with $I = 0.1$ mA.

ing transition starts at $T_c \approx 3$ K. However, the saturation is not seen down to 1.8 K, probably due to temperature limitations of the device.

The inset of Fig. 7(a) presents the metallic nature of resistivity as a function of temperature in cubic $PtBi_2$ with estimated RRR = 650. Figure 7(a) shows the temperature dependence of the normalized in-plane resistivity ρ/ρ_{290K} of the $Pt_{1-x}Rh_xBi_2$ crystals with $x = 0$ and $x = 0.35$. $PtBi_2$ presents a metallic behavior with a residual resistivity ratio (RRR) up to 132, evidencing the high purity of the sample. $Pt_{0.65}Rh_{0.35}Bi_2$ is also metallic, but its RRR decreases to 2.7 due to the disorder introduced by the Rh substitution.

Measurements at very low temperature show a broad superconducting transition at 600 mK for a current of 500 μA [Fig. 7(b)]. This superconducting transition disappears in the presence of a 500 mT magnetic field [Fig. 7(b)] and we measure a critical magnetic field B_c [defined as $R(Bc) = R_N/2$, with R_N being the resistance in the normal state] of 60 mT [Fig. 7(c)]. Further details regarding superconductivity anisotropy are reported elsewhere [33]. Similar transitions are observed in the $Pt_{0.65}Rh_{0.35}Bi_2$ doped crystals, but with a significantly larger critical temperature of 2.75 K for a current of 0.1 mA [see Fig. 7(a) and the inset in Fig. 7(b)], which is in line with magnetization measurements. Again, a magnetic field of 1 T aligned along the c axis at a temperature of 1 K suppresses this superconducting transition [inset of Fig. 7(b)]. By increasing the current, the transition systematically broadens [Fig. 7(d) for $Pt_{0.65}Rh_{0.35}Bi_2$, consistently with a progressive suppression of the superconducting phase (the not-well-defined geometry of the sample did not allow a reliable estimation of the critical current). As expected for the superconducting state, the superconductivity is weakened by increasing the temperature and the critical field decreases accordingly. In the inset of Fig. 7(d), the field dependence of ρ/ρ_{290K} is also presented: with increasing the temperature, the critical field, required to suppress the superconducting phase, diminishes as expected.

C. Electronic band structure calculation

Figure 8(b) shows the electronic density of states (DOS). The density of states shows a minimum for the stoichiometric compound at the Fermi level. Close to the Fermi level, only 6p Bi and 5d Pt states are present. The orbital projected band structure is presented in Fig. 8(a) and the corresponding Fermi surface is shown in Fig. 8(c). The color map in the figure shows the velocity of the corresponding groups of electrons at the Fermi level. The obtained band structure agrees with the

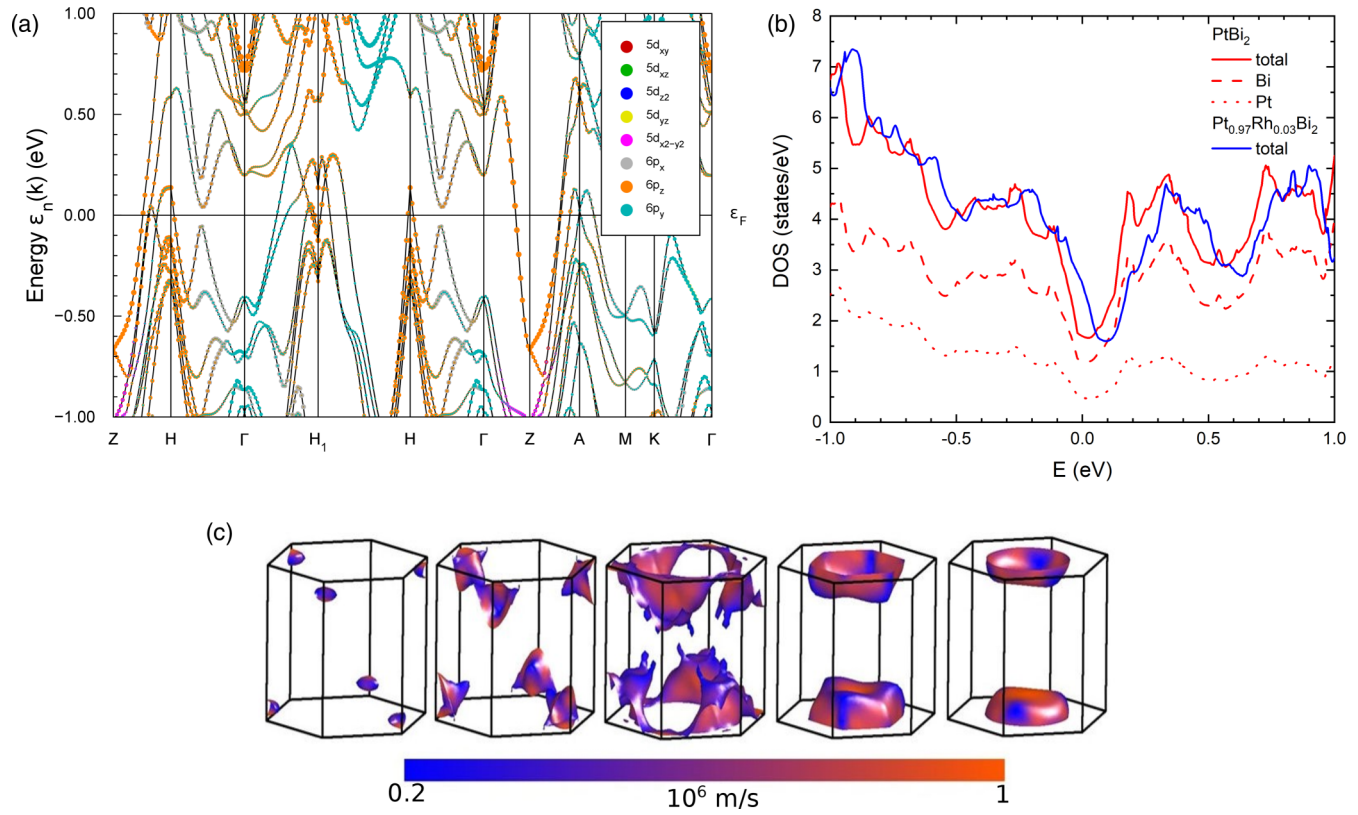

FIG. 8. (a) Orbital decomposed band structure of trigonal $PtBi_2$, showing the contribution of 5*d* Pt and 6*p* Bi orbitals. (b) Total DOS for trigonal $PtBi_2$ and partial contribution of Pt and Bi orbitals and DOS in $Pt_{0.97}Rh_{0.03}Bi_2$. (c) Fermi surface of trigonal $PtBi_2$.

one reported earlier [24]. The substitution of Pt by Rh leads to hole doping and enhancement of the DOS at the Fermi level. The rise of the superconducting critical temperature with Rh doping may be attributed to this DOS enhancement.

IV. CONCLUSION

In summary, we have successfully grown single crystals of both trigonal and pyrite-type polymorphic modifications of $PtBi_2$, as well as trigonal $Pt_{1-x}Rh_xBi_2$ for $x = 0.03$ and 0.35 via the self-flux technique. As-grown crystals were carefully characterized by SEM/EDX, powder x-ray diffraction and SAED. The pyrite type crystallizes in the FeS_2 structure type with space group $Pa\bar{3}$, whereas the trigonal modification crystallizes in the $P31m$ space group as opposed to $P\bar{3}$. Further, we have successfully grown the single crystals of Rh-doped $PtBi_2$ in trigonal modification, which also shows a $Pt_{1-x}Rh_xBi_2$ solid solution formation. Structural characterization demonstrates that the crystal structure is preserved up to at least $x = 0.35$. Resistivity measurements for as-grown crystals show a metallic nature. For pristine trigonal $PtBi_2$, the superconducting transition is found at 600 mK. For the $x = 0.35$ compound as measured, the superconducting transition temperature is enhanced up to 2.7 K compared to pristine $PtBi_2$ from both resistivity as well as from susceptibility measurements, which is in line with the DOS shift near the Fermi level according to the calculations. Our findings, together with data previously published, make the $PtBi_2$ family of materials a strong candidate for topological superconductivity. This finding warrants further research using techniques such as quantum transport and scanning tunneling microscopy, and the effect of the substitution on the nontrivial band structure of the compound should be further investigated by revisiting the electronic structure measurements using ARPES.

The datasets analyzed during the current study are available from the corresponding authors upon reasonable request.

ACKNOWLEDGMENTS

S.A. acknowledges the support of Deutsche Forschungsgemeinschaft (DFG) through Grant No. AS 523/4–1. S.A., D.V.E., and B.B. also acknowledge the support of DFG through Project No. 405940956. I.K. and B.B. acknowledge the support of BMBF through UKRATOP (BMBF), Grant No. FKZ: 01DK18002. J.D. acknowledges financial support by the Deutsche Forschungsgemeinschaft (DFG) through the SPP 1666 Topological Insulators program and the Würzburg-Dresden Cluster of Excellence on Complexity and Topology in Quantum Matter — ct.qmat (EXC 2147, Project ID No. 39085490). A.L., D.W., and S.S. acknowledge funding from DFG SFB 1415, Project ID No. 417590517. This project has received funding from the European Research Council (ERC) under the European Union's Horizon 2020 research and innovation programme (Grant Agreement No. 647276-MARS-ERC-2014-CoG).

The authors declare no competing financial or nonfinancial interests.

[1] S. R. Lee, P. A. Sharma, A. L. Lima-Sharma, W. Pan, and T. M. Nenoff, Topological quantum materials for realizing Majorana quasiparticles, Chem. Mater. **31**, 26 (2019).

[2] N. Savage, Topology shapes a search for new materials, ACS Central Sci. **4**, 523 (2018).

[3] B. Yan and C. Felser, Topological materials: Weyl semimetals, Annu. Rev. Condens. Matter Phys. **8**, 337 (2017).

[4] S.-Y. Xu, I. Belopolski, N. Alidoust, M. Neupane, G. Bian, C. Zhang, R. Sankar, G. Chang, Z. Yuan, C.-C. Lee *et al.*, Discovery of a Weyl fermion semimetal and topological Fermi arcs, Science **349**, 613 (2015).

[5] S. Borisenko, Q. Gibson, D. Evtushinsky, V. Zabolotnyy, B. Büchner, and R. J. Cava, Experimental Realization of a Three-Dimensional Dirac Semimetal, Phys. Rev. Lett. **113**, 027603 (2014).

[6] C. Shekhar, A. K. Nayak, Y. Sun, M. Schmidt, M. Nicklas, I. Leermakers, U. Zeitler, Y. Skourski, J. Wosnitza, Z. Liu *et al.*, Extremely large magnetoresistance and ultrahigh mobility in the topological Weyl semimetal candidate NbP, Nat. Phys. **11**, 645 (2015).

[7] T. Liang, Q. Gibson, M. N. Ali, M. Liu, R. J. Cava, and N. P. Ong, Ultrahigh mobility and giant magnetoresistance in the dirac semimetal Cd_3As_2, Nat. Mater. **14**, 280 (2015).

[8] F. Arnold, C. Shekhar, S.-C. Wu, Y. Sun, R. D. Dos Reis, N. Kumar, M. Naumann, M. O. Ajeesh, M. Schmidt, A. G. Grushin *et al.*, Negative magnetoresistance without well-defined chirality in the Weyl semimetal TaP, Nat. Commun. **7**, 11615 (2016).

[9] A. A. Zyuzin and R. P. Tiwari, Intrinsic anomalous Hall effect in type-II Weyl semimetals, JETP Lett. **103**, 717 (2016).

[10] A. Vaezi, Fractional topological superconductor with fractionalized Majorana fermions, Phys. Rev. B **87**, 035132 (2013).

[11] N. E. Alekseevski and Yu. P. Gaidukov, Zh. Eksp. Teor. Fiz. **25**, 383 (1953).

[12] H. Okamoto, The Bi-Pt (bismuth-platinum) system, J. Phase Equilib. **12**, 207 (1991).

[13] N. Zhuravlev and A. Stepanova, An x-ray investigation of superconducting alloys of bismuth with platinum in the range 20–640° C, Sov. Phys. Crystallogr. **7**, 241 (1962).

[14] T. Biswas and K. Schubert, Structural investigation in the mixtures Pt-Tl-Pb and Pt-Pb-Bi, J. Less-Common Met. **19**, 223 (1969).

[15] W. Gao, N. Hao, F.-W. Zheng, W. Ning, M. Wu, X. Zhu, G. Zheng, J. Zhang, J. Lu, H. Zhang *et al.*, Extremely Large Magnetoresistance in a Topological Semimetal Candidate Pyrite $PtBi_2$, Phys. Rev. Lett. **118**, 256601 (2017).

[16] Q. D. Gibson, L. M. Schoop, L. Muechler, L. S. Xie, M. Hirschberger, N. P. Ong, R. Car, and R. J. Cava, Three-dimensional dirac semimetals: Design principles and predictions of new materials, Phys. Rev. B **91**, 205128 (2015).

[17] X. Chen, D. Shao, C. Gu, Y. Zhou, C. An, Y. Zhou, X. Zhu, T. Chen, M. Tian, J. Sun, and Z. Yang, Pressure-induced multiband superconductivity in pyrite $PtBi_2$ with perfect electron-hole compensation, Phys. Rev. Mater. **2**, 054203 (2018).

[18] S. Thirupathaiah, Y. S. Kushnirenk, K. Koepernik, B. R. Piening, B. Buechner, S. Aswartham, J. van den Brink, S. V. Borisenko, and I. C. Fulga, Sixfold fermion near the Fermi level in cubic $PtBi_2$, arXiv:2006.08642.

[19] X. Yang, H. Bai, Z. Wang, Y. Li, Q. Chen, J. Chen, Y. Li, C. Feng, Y. Zheng, and Z.-A. Xu, Giant linear magneto-resistance in nonmagnetic $PtBi_2$, Appl. Phys. Lett. **108**, 252401 (2016).

[20] S. Thirupathaiah, Y. Kushnirenko, E. Haubold, A. V. Fedorov, E. D. L. Rienks, T. K. Kim, A. N. Yaresko, C. G. F. Blum, S. Aswartham, B. Büchner, and S. V. Borisenko, Possible origin of linear magnetoresistance: Observation of dirac surface states in layered $PtBi_2$, Phys. Rev. B **97**, 035133 (2018).

[21] Q. Yao, Y. P. Du, X. J. Yang, Y. Zheng, D. F. Xu, X. H. Niu, X. P. Shen, H. F. Yang, P. Dudin, T. K. Kim, M. Hoesch, I. Vobornik, Z.-A. Xu, X. G. Wan, D. L. Feng, and D. W. Shen, Bulk and surface electronic structure of hexagonal structured $PtBi_2$ studied by angle-resolved photoemission spectroscopy, Phys. Rev. B **94**, 235140 (2016).

[22] C. Q. Xu, X. Z. Xing, X. Xu, B. Li, B. Chen, L. Q. Che, X. Lu, J. Dai, and Z. X. Shi, Synthesis, physical properties, and band structure of the layered bismuthide $PtBi_2$, Phys. Rev. B **94**, 165119 (2016).

[23] M. Kaiser, A. I. Baranov, and M. Ruck, Bi_2Pt(hP9) by low-temperature reduction of $Bi_{13}Pt_3I_7$: Reinvestigation of the crystal structure and chemical bonding analysis, Z. Anorg. Allg. Chem. **640**, 2742 (2014).

[24] W. Gao, X. Zhu, F. Zheng, M. Wu, J. Zhang, C. Xi, P. Zhang, Y. Zhang, N. Hao, W. Ning, and M. Tian, A possible candidate for triply degenerate point fermions in trigonal layered $PtBi_2$, Nat. Commun. **9**, 3249 (2018)

[25] N. E. Brese and H. G. von Schnering, Bonding trends in pyrites and a reinvestigation of the structures of $PdAs_2$, $PdSb_2$, $PtSb_2$ and $PtBi_2$, Z. Anorg. Allg. Chem. **620**, 393 (1994).

[26] P. C. Canfield, T. Kong, U. S. Kaluarachchi, and N. H. Jo, Use of frit-disc crucibles for routine and exploratory solution growth of single crystalline samples, Philos. Mag. **96**, 84 (2016).

[27] J. Rodríguez-Carvajal, Recent advances in magnetic structure determination by neutron powder diffraction, Phys. B: Condens. Matter **192**, 55 (1993).

[28] V. Petříček, M. Dušek, and L. Palatinus, Crystallographic computing system JANA2006: General features, Z. Kristallogr. Cryst. Mater. **229**, 345 (2014).

[29] K. Koepernik and H. Eschrig, Full-potential nonorthogonal local-orbital minimum-basis band-structure scheme, Phys. Rev. B **59**, 1743 (1999).

[30] J. P. Perdew, K. Burke, and M. Ernzerhof, Generalized Gradient Approximation Made Simple, Phys. Rev. Lett. **77**, 3865 (1996).

[31] A. Cortijo, D. Kharzeev, K. Landsteiner, and M. A. H. Vozmediano, Strain-induced chiral magnetic effect in Weyl semimetals, Phys. Rev. B **94**, 241405(R) (2016).

[32] F. C. Chen, X. Luo, R. C. Xiao, W. J. Lu, B. Zhang, H. X. Yang, J. Q. Li, Q. L. Pei, D. F. Shao, R. R. Zhang, L. S. Ling, C. Y. Xi, W. H. Song, and Y. P. Sun, Superconductivity enhancement in the s-doped Weyl semimetal candidate $MoTe_2$, Appl. Phys. Lett. **108**, 162601 (2016).

[33] A. Veyrat, V. Labracherie, D. L. Bashlakov, F. Caglieris, J. I. Facio, G. Shipunov, L. Graf, J. Schoop, R. Giraud, J. van den Brink, B. Büchner, C. Hess, S. Aswartham, and J. Dufouleur, Topology and two-dimensional superconductivity in trigonal $PtBi_2$ (2020) (unpublished).